Cancer-Associated Fibroblasts Suppress CD8$^+$ T-cell Infiltration and Confer Resistance to Immune-Checkpoint Blockade

Liam Jenkins[1,2], Ute Jungwirth[1,3], Alexandra Avgustinova[1], Marjan Iravani[1], Adam Mills[1], Syed Haider[1], James Harper[2], and Clare M. Isacke[1]

ABSTRACT

Immune-checkpoint blockade (ICB) promotes antitumor immune responses and can result in durable patient benefit. However, response rates in breast cancer patients remain modest, stimulating efforts to discover novel treatment options. Cancer-associated fibroblasts (CAF) represent a major component of the breast tumor microenvironment and have known immunosuppressive functions in addition to their well-established roles in directly promoting tumor growth and metastasis. Here we utilized paired syngeneic mouse mammary carcinoma models to show that CAF abundance is associated with insensitivity to combination αCTLA4 and αPD-L1 ICB. CAF-rich tumors exhibited an immunologically cold tumor microenvironment, with transcriptomic, flow cytometric, and quantitative histopathologic analyses demonstrating a relationship between CAF density and a CD8$^+$ T-cell–excluded tumor phenotype. The CAF receptor Endo180 (*Mrc2*) is predominantly expressed on myofibroblastic CAFs, and its genetic deletion depleted a subset of αSMA-expressing CAFs and impaired tumor progression *in vivo*. The addition of wild-type, but not Endo180-deficient, CAFs in coimplantation studies restricted CD8$^+$ T-cell intratumoral infiltration, and tumors in Endo180 knockout mice exhibited increased CD8$^+$ T-cell infiltration and enhanced sensitivity to ICB compared with tumors in wild-type mice. Clinically, in a trial of melanoma patients, high *MRC2* mRNA levels in tumors were associated with a poor response to αPD-1 therapy, highlighting the potential benefits of therapeutically targeting a specific CAF subpopulation in breast and other CAF-rich cancers to improve clinical responses to immunotherapy.

Significance: Paired syngeneic models help unravel the interplay between CAF and tumor immune evasion, highlighting the benefits of targeting fibroblast subpopulations to improve clinical responses to immunotherapy.

Introduction

The therapeutic blockade of immune-checkpoint proteins such as cytotoxic T-lymphocyte associated antigen-4 (CTLA4) and programmed death ligand-1 (PD-L1) promotes antitumor immunity and confers a durable clinical benefit in a subset of cancer patients (1). Clinical responses to ICB are observed in multiple cancer types, but are often restricted to patients whose tumors are highly mutated, express high levels of PD-L1, and are infiltrated by a sufficiently diverse repertoire of tumor-specific CD8$^+$ T cells (2, 3). Breast cancers, which commonly lack these features, have long been considered immunologically silent and not amenable to ICB treatment. Nevertheless, evidence associating lymphocytic infiltration with better prognosis in both triple-negative breast cancer (TNBC) and HER2$^+$ disease (4), has prompted exploration of ICB as a treatment option in numerous clinical trials.

Following the reporting of the KEYNOTE-522 and -355 trials (5, 6), the FDA granted approval for the PD-L1 inhibitor pembrolizumab in combination with chemotherapy for the treatment of patients with advanced TNBC whose tumors are PD-L1 positive, and for high-risk early-stage TNBC as neoadjuvant treatment with continued use as single-agent adjuvant treatment following surgery. However, despite these advances, only a proportion of breast cancer patients treated with ICB therapy experience durable responses, even when considering mutational status or checkpoint inhibitor expression (7). Thus, elucidating the determinants of ICB response will be key to developing new treatment strategies that potentiate antitumor immune responses and improve outcomes in patients for whom ICB treatment is not currently effective.

Accumulating evidence has demonstrated that the overall proportion, phenotype, and distribution of immune cells within the tumor microenvironment (TME) are important in determining responses to ICB (4, 7). Indeed, patients with immunologically hot tumors, characterized by PD-L1 expression and CD4$^+$ and CD8$^+$ T cells positioned in proximity to tumor cells, exhibit better responses to anti–PD-L1/PD-1 therapy than those whose tumors are characterized by a paucity of these effector populations or an "immune-excluded" phenotype (8). CAFs, a major constituent of the breast TME, are a heterogeneous population of cells with an emerging role in modulating antitumor immunity and influencing responses to treatment (9–14). CAFs directly contribute to tumor growth, metastasis, and angiogenesis, but may also promote the establishment of an immunologically cold

[1]The Breast Cancer Now Toby Robins Research Centre, The Institute of Cancer Research, London, UK. [2]Early Oncology R&D, AstraZeneca, Aaron Klug Building, Granta Park, Cambridge, UK. [3]Department of Pharmacy and Pharmacology, Centre for Therapeutic Innovation, University of Bath, Bath, UK.

Current address for A. Avgustinova: Institut de Recerca Sant Joan de Déu, Carrer Santa Rosa 39-57, 08950 Esplugues de Llobregat, Spain.

Corresponding Author: Clare M. Isacke, The Breast Cancer Now Toby Robins Research Centre, The Institute of Cancer Research, 237 Fulham Road, London SW3 6JB, UK. Phone: 44-20-7153 5510; E-mail: clare.isacke@icr.ac.uk

Cancer Res 2022;82:2904–17

doi: 10.1158/0008-5472.CAN-21-4141

tumor phenotype, either through direct inhibition of T-cell infiltration and activity or by promoting recruitment of other immunosuppressive cell types.

Despite these advances, studies investigating the relationship between CAFs and antitumor immunity have been stifled by the well-documented variability between CAFs in different cancers, the lack of specific CAF markers, and the paucity of suitable preclinical models (15). Here we have utilized paired syngeneic mouse mammary carcinoma models that differ in their CAF abundance to better characterize the relationship between CAF prevalence, immunomodulation, and sensitivity to ICB. We demonstrate that CAF-rich tumors exhibit an immunologically cold, $CD8^+$ T-cell–excluded TME and that targeting CAF subsets via genetic deletion or downregulation of the myofibroblastic CAF (myCAF) restricted receptor Endo180 (*Mrc2*) facilitates $CD8^+$ T-cell infiltration and enhances sensitivity to ICB, findings corroborated in human clinical samples where high Endo180 expression is associated with poor responses to αPD-1. Given the heightened interest in using immunotherapy to treat breast cancer, together with the improved understanding of the diversity of CAF biology, targeting Endo180 offers a novel CAF-associated approach to improving ICB responses.

Materials and Methods

Reagents and cells

Cells were from Isacke laboratory stocks and were subjected to *Mycoplasma* testing (MycoAlert Mycoplasma Detection Kit, Lonza) on a monthly basis and used within eight passages of thawing. Adherent cells were cultured at 37°C in a tissue culture incubator with humidified air, supplemented with CO_2 to 5%. Unless otherwise stated, cells were maintained in DMEM plus 10% FBS and 1% penicillin/streptomycin. D2A1 cells were provided by Ann Chambers (University of Western Ontario). The generation of the metastatic D2A1-m2 subline, and D2A1 and D2A1-m2 cells expressing mCherry and luciferase2 have been described previously (16, 17). Whole-exome sequencing of cell lines was performed and analyzed as described previously (16).

GFP^+ normal mammary fibroblasts (NMF) and 4T1 tumor-derived CAFs were isolated from Ub-GFP BALB/c mice (18), as previously described (16). CAFs were immortalized using an HPV-E6/E7-puromycin retrovirus (provided by Fernando Calvo). NMFs were immortalized using an HPV-E6/E7-neomycin lentivirus (Applied Biological Materials). Primary fibroblasts were incubated with virus-containing media (1:1 dilution with fresh complete media plus 8 μg/mL polybrene) for 48 hours. CAFs transduced with nontargeting or Endo180 targeting shRNAs have been described previously (16).

Antibodies, and the dilutions used, are detailed in Supplementary Table S1.

Cellular assays

For T-cell proliferation experiments, spleens from naïve BALB/c mice were dissociated through 40-μm filters. After red blood cell lysis, T cells were isolated using the EasySep mouse T-cell isolation kit, labeled with 1 mmol/L CFSE, and plated in complete RPMI media supplemented with 50 mmol/L β-mercaptoethanol into 96-well plates coated with 1 μg/mL αCD3e antibody. Naïve CFSE-stained T cells were cultured for 4 days at 37°C with 5 μg/mL αCD28 antibody and 10 ng/mL IL2 (BD Biosciences) in complete RPMI media or CAF-conditioned complete RPMI media. A conditioned medium was generated by culturing CAFs in a complete medium for 72 hours and filtering through a 40-μm filter. After 4 days, cells were stained with an anti-mouse CD16/CD32 antibody for 10 minutes at room temperature to block the nonspecific binding of staining antibodies. APC-conjugated αCD45, PE-conjugated αCD4, and PerCP/Cy5.5-conjugated αCD8 antibodies were added to cells at specified dilutions (Supplementary Table S1) and incubated at 4°C for 30 minutes. Cells were stained with DAPI, and the CFSE signal in gated live $CD4^+$ and $CD8^+$ T cells was measured by flow cytometry (LSRII flow cytometer, BD Biosciences).

For PD-L1 expression analysis, cells were cultured with 10 ng/mL recombinant mouse IFNγ (BioLegend). After 24 hours, cells were stained on coverslips and imaged on a Leica SP8 confocal microscope or detached and stained with an APC-conjugated αPD-L1 antibody, or an isotype control antibody. Live cells (DAPI-negative) were assessed for PD-L1 expression by flow cytometry (LSRII flow cytometer, BD Biosciences).

In vivo procedures

All animal work was carried out under UK Home Office Project Licenses 70/7413, P6AB1448A, and PP4856884 granted under the Animals (Scientific Procedures) Act 1986 (Establishment Licence, X702B0E74 70/2902) and was approved by the "Animal Welfare and Ethical Review Body" at The Institute of Cancer Research (ICR). Mice with a genetic deletion in Endo180 (*Mrc2*; ref. 19) were backcrossed for at least six generations with BALB/c (Charles River) mice. Genotypes were confirmed by PCR. All mice were housed in individually ventilated cages, monitored daily by ICR Biological Services Unit staff, and had food and water *ad libitum*. Mice were weighed at least two times per week.

Tumor cells (5×10^5 4T07, 5×10^4 4T1, 2×10^5 D2A1, or 2×10^5 D2A1-m2) were implanted in PBS orthotopically into the fourth mammary fat pad of 6- to 8-week-old female BALB/c or NOD scid gamma (NSG) mice (Charles River) under general anesthesia. 4T07 and D2A1 cells were either implanted alone or mixed with 6×10^5 NMFs or CAFs. Tumor growth was measured every 2 to 3 days, and tumor volume was calculated as $0.5236 \times [(\text{width} + \text{length})/2]^3$. Tumor growth rates were calculated as previously described (20).

For immune-checkpoint blockade treatment, mice received, via intraperitoneal injection, 10 mg/kg of αCTLA4 or αPD-L1 antibodies (Supplementary Table S1) either as single agents or in combination. Control mice received 10 mg/kg of respective mouse IgG_1 kappa and/or IgG_1 D265A isotype control antibodies. Unless otherwise stated, αCTLA4 was given on days 7, 11, 14, 18, 21, and 25 after cell implant, and αPD-L1 was given on days 5, 7, 11, 14, 18, and 21 after cell implantation. Mice were culled individually when tumors reached 17 mm in diameter (survival analysis) or culled as a group when the first tumor reached 17 mm in diameter (tumor growth analysis).

Histology

For αSMA and CD8 IHC, tissues were removed and fixed overnight at room temperature in 4% paraformaldehyde and embedded in paraffin wax after processing in a Tissue-Tek VIP automatic tissue processor. Sections (3–4 μm) were cut from formalin-fixed paraffin-embedded tissue blocks, dewaxed in xylene, rehydrated through ethanol washes, and stained using hematoxylin and eosin or subjected to high-temperature antigen retrieval, depending on primary antibody requirements. Slides were cooled at room temperature before incubation with antibodies. Stained sections were scanned on the NanoZoomer Digital Pathology (Hamamatsu). All images were quantified in a blinded fashion. αSMA staining was analyzed in ImageJ from ≥ 6 randomly selected 1 mm^2 fields of view per tumor section. HRP images were color deconvoluted using the ImageJ H DAB vector and

converted into 8-bit images, and the percentage of the αSMA-stained area was quantified in a blinded fashion (threshold, 0–130). The same thresholding was applied to all images from the same experiment. For quantitative spatial analysis of $CD8^+$ cell infiltration, QuPath software (21) was used to count the number of positively stained cells in eight randomly selected peripheral and eight central 1-mm^2 regions of tumor tissue. To examine intratumoral heterogeneity, 0.25 mm^2 matched regions from serial αSMA- and CD8-stained sections were selected and quantified as described above. For all IHC quantification, areas of necrosis were avoided, and the data shown are mean values per tumor section.

Tumor dissociation and flow cytometry

For analysis of tumor-infiltrating immune cells, tumors were removed, and single-cell suspensions were generated using a tumor dissociation kit in combination with a gentleMACS Octo Dissociator with the program 37C_m_TDK_2 according to the manufacturer's protocol (Miltenyi Biotec). Samples were subsequently applied to a 70-μm MACS SmartStrainer and washed in PBS and incubated in RBC lysis buffer (Sigma) for 5 minutes at room temperature. Samples were resuspended in FACS buffer for staining.

Single-cell suspensions were stained with Fixable Viability Dye eFluor 455UV (Thermo Fisher Scientific) for 20 minutes at 4°C. Cells were subsequently stained with an anti-mouse CD16/CD32 antibody for 10 minutes at room temperature to block nonspecific binding to Fc receptor–expressing cells. Panels of directly conjugated antibodies against cell-surface markers were added to cell suspensions at specified dilutions and incubated at 4°C for 30 minutes. Cells were washed twice in PBS before being fixed and permeabilized overnight using the FoxP3/Transcription factor staining buffer set (eBioscience). Panels of directly conjugated antibodies against intracellular markers were then added to cells for 60 minutes at 4°C. Following further washing, cells were fixed in 4% paraformaldehyde solution for 15 minutes at 4°C. Finally, cells were resuspended in FACS buffer and analyzed on a BD LSRFortessa or BD LSRII flow cytometer. Stained cells or fluorescent UltraComp eBeads (eBioscience 01-2222) were used for compensation setup. Data analysis was performed using FlowJo software (Tree Star Inc.). Gates were set using appropriate fluorescence minus one controls.

NanoString profiling of tumors

Tumors were harvested and snap frozen in liquid nitrogen. Frozen tissue was lysed in RLT buffer (Qiagen) containing 1/100 β-mercaptoethanol in Hard-Tissue homogenizing CK28 tubes and homogenized using a Precellys tissue homogenizer (Bertin-Corp) for 2 minutes. RNA was extracted and purified using the Qiagen RNeasy kit according to the manufacturer's protocol. RNA was hybridized with the NanoString PanCancer mouse immune-oncology (IO) 360 Panel. Raw NanoString data were preprocessed using R package NanoStringNorm (v1.2.1). Differential mRNA abundance analysis was performed using voom (TMM normalization), with R package limma (v3.34.9; ref. 22). Genes with an absolute $\log_2$ fold change of >1 and an adjusted P of <0.05 were considered significant. For immune cell population abundance analysis, NanoString-curated genesets representing specific cell types were used. For each cell type, genesets with more than two genes were further reduced to the largest positively correlated cluster of genes by running hierarchical clustering on Spearman correlation distance, followed by the identification of an optimal number of clusters using the Silhouette score. Genes were kept if they all showed pairwise Spearman $P > 0.5$. A similar approach was used for the comparison of CD8 T effector (NanoString), fibroblast TGFβ response signature (F-TBRS; ref. 23), TGFβ Signaling (NanoString), and Wnt Signaling signatures (NanoString). All analyses were performed in R statistical programming language (v3.4.4).

The Cancer Genome Atlas breast cancer cell type abundance estimates

Using The Cancer Genome Atlas (TCGA) breast cancer (BRCA) RNA-seq profiles (RSEM normalized; ref. 24), relative cell type abundance estimates were created using the Consensus^{TME} (25). The statistical metric used for the estimation of scores was set to *ssgsea*. Hierarchical clustering was performed on both rows and columns using "euclidean" as the distance measure and "complete" as the agglomeration method. The association between the cell type abundance estimates and selected marker genes was computed using the Spearman rank correlation.

Analysis of data sets

Anti–PD-1 immunotherapy trial: Preprocessed RNA-seq profiles of pretreatment melanomas (26) were downloaded from GEO identifier GSE78220. Differential gene expression for selected marker genes in anti–PD-1 nonresponders (patients with progressive disease) and responders (complete or partial response) was assessed using an unpaired nonparametric Wilcox rank-sum test. Single-cell RNA-seq (scRNA-seq): scRNA-Seq data from 26 human breast cancers (27) were visualized on the Broad Institute Single-Cell portal at https://singlecell.broadinstitute.org/single_cell/study/SCP1039.

Statistical analysis

Statistical tests were performed using GraphPad Prism 8. Unless otherwise indicated, data are presented as ± standard error of the mean, and comparisons between two groups were made using two-tailed, unpaired Student *t* test. If more than two groups were compared, one-way ANOVA analysis was performed with Dunnett test for multiple comparisons. For all correlation analysis, R^2 values were calculated from the Pearson correlation coefficient. For survival analysis, data were analyzed with a log-rank test, comparing only two groups at a time. Box plots show median and 25th–75th quartiles, whiskers show minimum and maximum. P values are reported as follows: $P \geq 0.05$ (ns, nonsignificant); *, $P < 0.05$; **, $P < 0.01$; ***, $P < 0.001$; ****, $P < 0.0001$.

Data availability

The whole-exome sequencing data have been deposited at the European Nucleotide Archive (ENA) and are available under the accession number PRJEB43908 (D2A1, SAMEA8418396; D2A1-m2, SAMEA8418398; normal BALB/c, SAMEA8418401). The NanoString data have been deposited at Zenodo at https://doi.org/10.5281/zenodo.647812.

Results

CAF abundance is associated with insensitivity to ICB

To investigate the role of CAFs in modulating the breast tumor immune microenvironment, and to determine whether CAFs influence responses to ICB, the paired BALB/c-derived, 4T1 and 4T07 mouse mammary carcinoma cell lines (28) were used. As previously reported (29), when implanted orthotopically into the mammary fat pad of syngeneic BALB/c mice, 4T1 cells give rise to primary tumors defined by an abundance of intratumoral αSMA^+ CAFs, whereas 4T07 tumors have significantly fewer (**Fig. 1A**; Supplementary Fig. S1A). Notably, 4T07 tumors grow poorly in immunocompetent BALB/c mice, either when implanted orthotopically (**Fig. 1B**) or subcutaneously

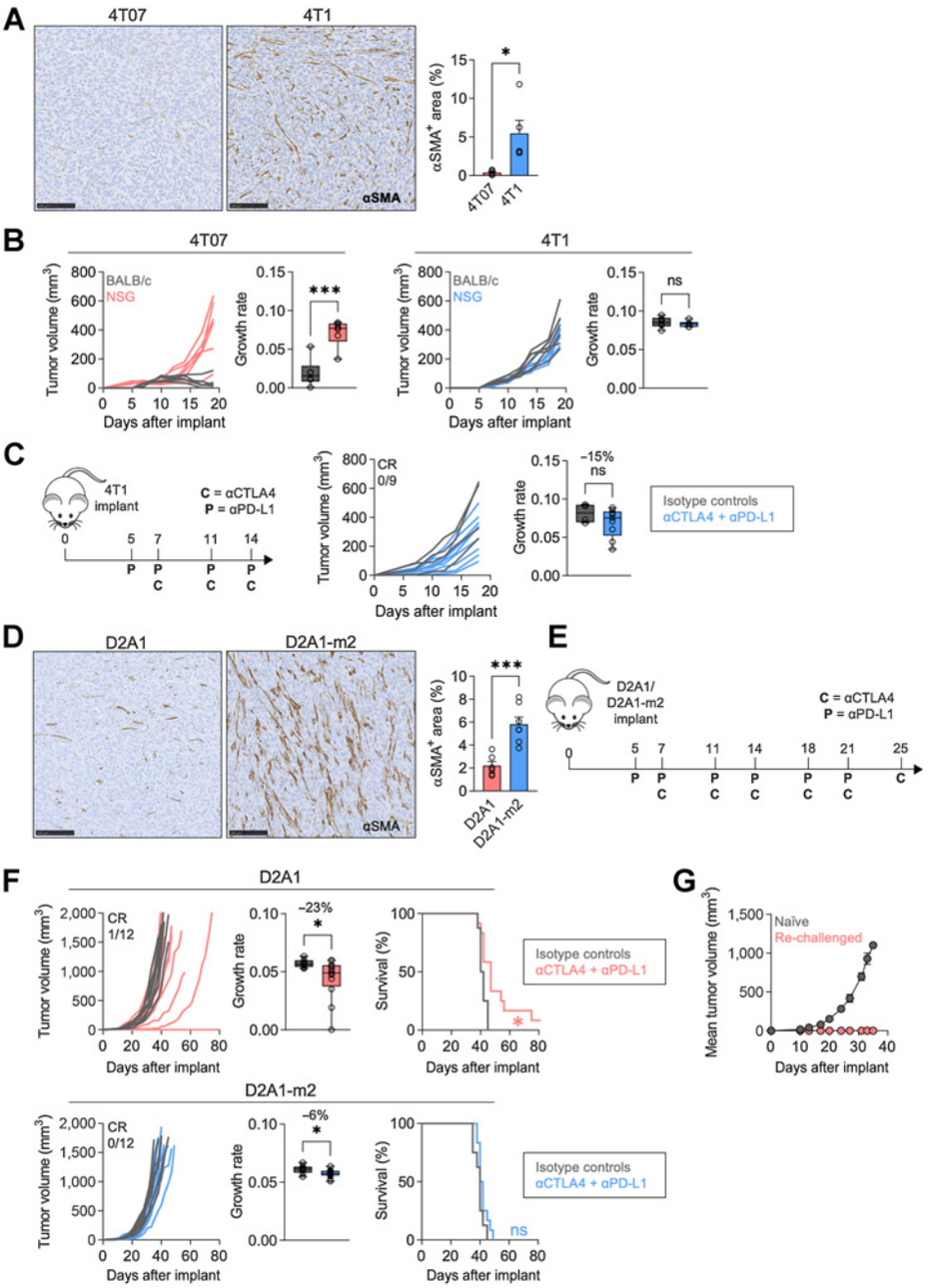

Figure 1.

CAF abundance is associated with insensitivity to ICB. **A,** 4T07 or 4T1 cells were implanted orthotopically into BALB/c mice ($n = 5$ per group). Mice were culled on day 17. Representative αSMA stained sections. Scale bar, 100 μm. Bar chart shows percentage of αSMA^+-stained area. **B,** 4T07 or 4T1 cells were implanted orthotopically into BALB/c or NSG mice ($n = 6$ per group). Tumor growth curves for individual mice and tumor growth rates. **C,** 4T1 cells were implanted orthotopically into BALB/c mice ($n = 4$–9 per group) and treated with αCTLA4 or αPD-L1 antibodies alone (see Supplementary Fig. S1C), or in combination, according to the schedule shown. Control mice received isotype control antibodies. Tumor growth curves for individual mice and tumor growth rates. **D,** D2A1 or D2A1-m2 cells were implanted orthotopically into BALB/c mice ($n = 6$ per group), and intratumoral αSMA staining was quantified as in **A**. **E** and **F,** D2A1 or D2A1-m2 cells were implanted orthotopically into BALB/c mice and treated with αCTLA4 and αPD-L1 antibodies in combination according to the schedule shown ($n = 8$ control and 12 ICB-treated mice per group). Tumor growth curves for individual mice (CR, complete responder), tumor growth rates, and Kaplan–Meier survival analysis (log-rank test). **G,** D2A1 cells were implanted bilaterally into naïve BALB/c mice ($n = 2$ mice) or into the opposite mammary fat pad of the surviving mouse from the D2A1 arm of **F** (rechallenged, $n = 1$ mouse). *, $P < 0.05$; ***, $P < 0.001$; ns, nonsignificant.

(Supplementary Fig. S1B), but grow readily in immunodeficient NSG mice (**Fig. 1B**). By contrast, 4T1 tumors exhibit similar growth kinetics in both strains (**Fig. 1B**), indicating that an intact immune response may be a major growth-restricting factor for 4T07, but not 4T1 tumors. Moreover, when NSG-derived 4T07 tumor fragments containing stromal components are transplanted into BALB/c mice, or when 4T07 cells are coimplanted with 4T1 tumor-derived CAFs, tumor growth is enhanced (Supplementary Fig. S1B and S1C), prompting us to investigate whether CAFs mediate this effect through inhibition of antitumor immunity.

As previously reported (30, 31), the 4T1 tumor model is largely insensitive to ICB, with single-agent αCTLA4 or αPD-L1 treatment promoting modest tumor growth inhibition, but ultimately failing to eradicate primary tumors (Supplementary Fig. S1D). Furthermore, despite clinical evidence suggesting that ICB combinations are more efficacious than single-agent treatment (32), combination αCTLA4 and αPD-L1 treatment fails to drive any complete tumor regression (**Fig. 1C**). Given the poor growth kinetics of 4T07 tumors in immunocompetent mice, the sensitivity of this model to ICB treatment could not be determined.

To further understand the relationship between CAFs and ICB sensitivity in additional syngeneic breast cancer models, the paired BALB/c-derived D2A1 mouse mammary carcinoma cell line and its metastatic D2A1-m2 subline (17) were examined. Orthotopic D2A1-m2 tumors are abundant in αSMA^+ CAFs, whereas parental D2A1 tumors are CAF-poor (**Fig. 1D**; Supplementary Fig. S1E). The sensitivity of both models to combination ICB treatment was assessed

using the dosing regimen outlined in **Fig. 1E**. In contrast to the 4T07/4T1 models, orthotopic implantation of BALB/c mice with either D2A1 or D2A1-m2 cells gives rise to primary tumors with similar and reproducible growth kinetics (**Fig. 1F**, isotype controls). Combined blockade of CTLA4 and PD-L1 has a limited effect on D2A1-m2 tumor growth rate (6% inhibition), with no statistically significant extension of median survival and no complete responders (**Fig. 1F**). By contrast, combination αCTLA4 and αPD-L1 treatment suppresses D2A1 tumor growth (23% growth rate inhibition) and significantly extends median survival from 41 to 47 days after tumor cell implantation (**Fig. 1F**), findings reproduced in an independent experiment (Supplementary Fig. S1F). One mouse exhibited complete tumor regression and developed an immunologic memory to D2A1 rechallenge, indicative of an adaptive antitumor immune response (**Fig. 1G**).

Insensitivity to ICB is independent of tumor cell–intrinsic factors

A high tumor mutational burden (TMB), defined as the number of nonsynonymous mutations per megabase (Mb) of total genomic DNA, drives neoantigen generation and is associated with improved ICB treatment response across multiple cancer types (2, 3). Whole-exome sequencing was used to identify cell-intrinsic genetic differences that may underlie the differential sensitivity of the D2A1 and D2A1-m2 models to ICB. Unsurprisingly, given that the D2A1-m2 subline is derived from parental D2A1 cells, when compared with a reference BALB/c mouse genome, the D2A1 and D2A1-m2 cells exhibit comparable copy-number variation profiles (**Fig. 2A**). Moreover, despite being less sensitive to ICB treatment, D2A1-m2 cells have a higher somatic nonsynonymous mutational burden (**Fig. 2B**). Many of these nonsynonymous mutations ($n = 206$) are shared, but the cell lines also carry distinct mutations (**Fig. 2C**), indicating that the D2A1 line comprises a heterogeneous population and that the D2A1-m2 cell subline likely diverges from the parental line during *in vivo* passage. Similar findings are observed when considering only exonic mutations in immune-related genes (**Fig. 2C**; Supplementary Table S2). The paucity of immune gene mutations, coupled with transcriptional profiling of the D2A1 and D2A1-m2 cell lines cultured *in vitro* failing to identify robust changes in immune regulators (17), indicates that differences in antitumor immune responses do not result from intrinsic mutational or transcriptional differences between these cell lines. Similarly, although flow cytometry analysis reveals significantly higher levels of PD-L1 on both immune and tumor cells within D2A1 tumors compared with D2A1-m2 tumors (**Fig. 2D**), in cultured D2A1 and D2A1-m2 cells, PD-L1 expression assessed by flow cytometry and immunostaining is similar at baseline (unstimulated) and following stimulation with IFNγ (**Fig. 2E** and **F**). These data indicate that elevated PD-L1 expression in D2A1 tumors reflects differences in immune activity within the TME, rather than intrinsic differences between the two cell lines.

αSMA$^+$ CAF abundance is associated with an immunologically cold TME

To explore further the characteristics of D2A1 and D2A1-m2 tumors underlying their differential sensitivity to ICB, we utilized the NanoString PanCancer mouse Immune-Oncology (IO) 360 gene expression panel to analyze the transcriptomes of established, untreated tumors of equivalent size (Supplementary Fig. S2A). Principal component analysis shows that D2A1 and D2A1-m2 tumors cluster separately (Supplementary Fig. S2B), and differential expression analysis reveals an elevated expression in D2A1-m2 tumors of numerous genes involved in fibroblast activation including *Wnt5a*, *Loxl2*, *Edn1*, *Inhba*, and *Wnt11* (**Fig. 3A**; Supplementary Fig. S2C). By contrast, the majority of genes with higher expression in D2A1 tumors have known roles in antitumor immunity, including chemoattractants such as *Cxcl9* and *Cxcl10*, and the interferon-inducible gene *Ifitm1*.

Unsupervised hierarchical cluster analysis using NanoString defined immune gene sets (Supplementary Fig. S2D) reveals clustering by tumor model (**Fig. 3B**) with D2A1-m2 tumors exhibiting a significantly lower abundance of total leukocytes (CD45), CD8$^+$ T cells, neutrophils and NK cells (**Fig. 3C**). Similarly, a clinically relevant gene set defining CD8$^+$ T effector cells that is associated with enhanced response to αPD-L1 treatment in metastatic urothelial carcinoma patients (Supplementary Fig. S2E; ref. 23) is expressed at significantly higher levels in D2A1 tumors (**Fig. 3D**), linking the effector function of tumor-infiltrating immune cells with sensitivity to ICB. Interestingly, the abundance of regulatory T cells (Treg) and macrophages, both cell types with an ability to suppress T-cell recruitment and function (33, 34), does not significantly differ between models, suggesting that they do not directly contribute to the lack of effector immune cell activity observed in D2A1-m2 tumors (**Fig. 3E**). Finally, we examined the expression of signatures associated with stromal activation (Supplementary Fig. S2E). Consistent with the IHC analysis of the tumor stroma (**Fig. 1D**), D2A1-m2 tumors exhibit an elevated expression of fibroblast activation signatures, exemplified by a fibroblast TGFβ response signature (F-TBRS) associated in both experimental models and clinical samples with an immune exclusion phenotype (23), and the NanoString TGFβ and Wnt signaling signatures (**Fig. 3F**). When considering all tumors, these TGFβ and fibroblast activation signatures were associated with a lower abundance of CD8$^+$ T-cell transcripts (**Fig. 3G**).

To confirm that αSMA$^+$ CAF abundance is associated with an immunologically cold TME, 4T07/4T1 and D2A1/D2A1-m2 primary tumors were assessed for their immune cell content via both flow cytometry and IHC. To control for temporal changes in immune cell composition, tumors were collected simultaneously, resulting in analysis of 4T1 tumors that were larger than 4T07 tumors, while D2A1 and D2A1-m2 tumors were of a similar size (Supplementary Fig. S3A). Consistent with the NanoString profiling, CAF-rich D2A1-m2 tumors contain fewer CD8$^+$ T cells compared with CAF-poor D2A1 tumors (**Fig. 4A** and **B**; Supplementary Fig. S3B). Equivalent findings were obtained with CAF-rich 4T1 and CAF-poor 4T07 tumors, with 4T1 tumors showing a significant reduction in CD8$^+$ T-cell content (**Fig. 4C** and **D**). Moreover, in intratumoral analysis, regions of high αSMA$^+$ cell abundance are significantly lower in CD8$^+$ T cells (**Fig. 4E**), together implicating a role for αSMA$^+$ CAFs in limiting CD8$^+$ T-cell content. In addition to the paucity of CD8$^+$ T cells, immunologically cold tumors are also characterized by T cells that lack expression of markers of cytotoxicity, such as granzyme B, and activation, such as PD-1 (35). Phenotypic flow cytometry analysis reveals that CAF-rich D2A1-m2 and 4T1 tumors contain fewer granzyme B and PD-1-expressing CD8$^+$ T cells than the CAF-poor D2A1 and 4T07 tumors (**Fig. 4F** and **G**). Despite these marked differences in CD8$^+$ T-cell abundance and activity, consistent with earlier transcriptomic analysis (**Fig. 3E**), immunologically colder D2A1-m2 and 4T1 tumors are no more abundant in cells with recognized immunosuppressive functions including Tregs, macrophages, and neutrophils (Supplementary Fig. S3C).

To address directly the role of CAFs in modulating the CD8$^+$ T-cell content of tumors, GFP$^+$ CAF cultures were generated from orthotopic 4T1 tumors grown in Ub-GFP BALB/c mice (Supplementary Fig. S4A). Sorted cells express the fibroblast markers αSMA, PDGFRα,

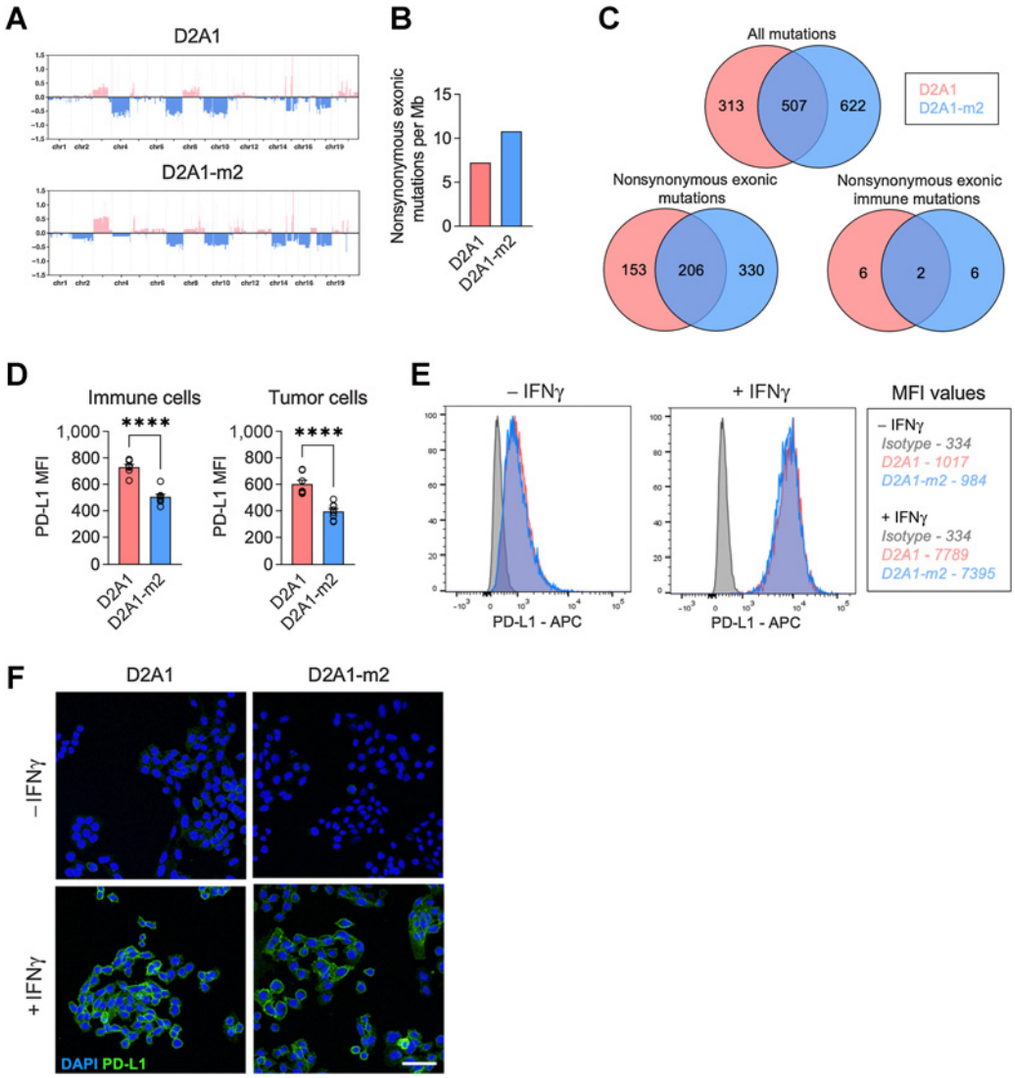

Figure 2.

Insensitivity to ICB *in vivo* is independent of tumor cell–intrinsic factors. D2A1 and D2A1-m2 cell lines and BALB/c mouse germline DNA (as reference) were subjected to whole-exome sequencing. **A,** Copy-number variation plots (log_2 ratio). **B,** Number of exonic nonsynonymous mutations per megabase (Mb) of exome. **C,** Venn diagrams illustrating the number of total mutations, nonsynonymous exonic mutations, and nonsynonymous exonic immune mutations in common between the D2A1 and D2A1-m2 cell lines. Immune mutations refer to mutations in the 750 genes represented in the NanoString mouse PanCancer IO 360 panel (see Supplementary Table S2). **D,** PD-L1 expression in $CD45^+$ immune cells and $CD45^-$ tumor cells from dissociated tumors [maximum fluorescence intensity (MFI) values]. **E** and **F,** Cultured cells with or without IFNγ stimulation were stained with APC-conjugated αPD-L1 or isotype control antibody and analyzed via flow cytometry (**E**) or stained *in situ* with αPD-L1 antibody, followed by Alexa488-conjugated anti-rat Ig and visualized by confocal microscopy (**F**). Scale bar, 50 μm. ****, $P < 0.0001$.

and Thy1.2 (CD90.2; ref. 36), but not the immune cell marker CD45 (Supplementary Fig. S4B). As previously reported by others (11), fibroblast conditioned media significantly inhibits *in vitro* proliferation of both $CD4^+$ and $CD8^+$ T cells (Supplementary Fig. S4C and S4D). Moreover, as previously observed with the 4T07 model (Supplementary Fig. S1C), coimplantation of D2A1 tumor cells with CAFs, but not NMFs, promotes tumor growth (**Fig. 5A**). Neither NMFs nor CAFs form tumors when implanted alone into syngeneic BALB/c mice (data not shown). As reported recently in a CAF "Consensus Statement" (15), an issue with this approach is that host-derived fibroblasts outgrow coimplanted CAFs during tumor development limiting their utility in longer-term efficacy studies. Indeed GFP^+ cells represent a relatively minor proportion of live cells within these tumors, while the proportion of $CD45^-$ $Thy1.2^+$ cells is higher (**Fig. 5B**; Supplementary Fig. S4E). Nevertheless, flow cytometry analysis of the immune cell composition reveals that coimplantation of D2A1 tumors cells with CAFs, but not NMFs, results in reduced $CD8^+$ T-cell levels (**Fig. 5B**) and while not significant, across all tumors there was a significant inverse correlation between the abundance of intratumoral CAFs and $CD8^+$ T cells (**Fig. 5C**), as observed in the D2A1/D2A1-m2 and 4T07/4T1 models (**Figs. 3G** and **4E**). Interestingly, in contrast to the fibroblast-mediated inhibition of T-cell proliferation

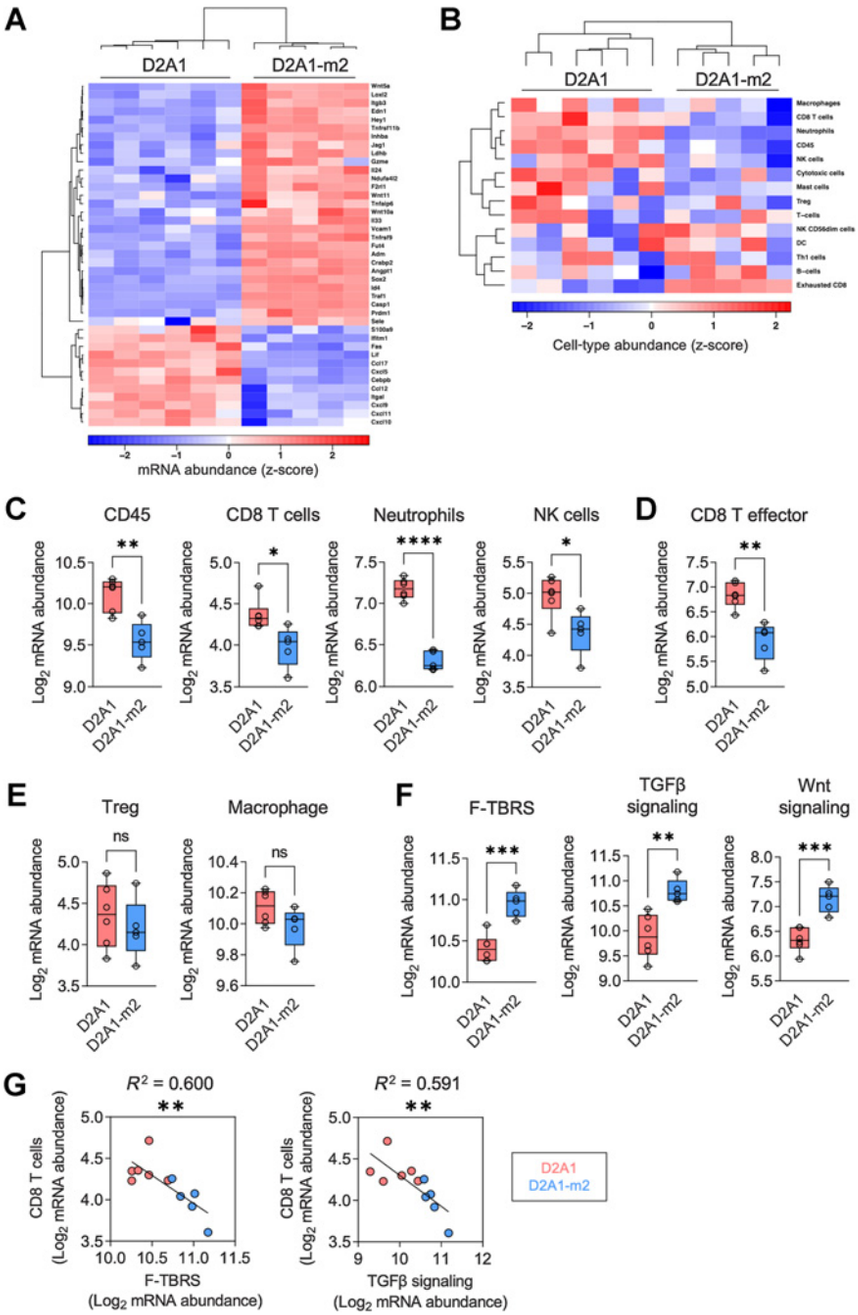

Figure 3.

NanoString transcriptomic profiling. D2A1 or D2A1-m2 cells were implanted orthotopically into BALB/c mice ($n = 5$ or 6 per group). Mice were culled on day 24 (see Supplementary Fig. S2A for tumor weights). **A,** Profiling of tumors was performed using the NanoString mouse IO 360 panel. Heatmap of significant differentially expressed genes. **B,** Unsupervised hierarchical clustering based on the expression of NanoString immune cell population abundance signatures (see Supplementary Fig. S2D). **C,** Significantly differentially expressed NanoString immune cell population abundance signatures. **D,** CD8 T effector signature expression. **E,** Treg and macrophage signature expression. **F,** Expression of fibroblast TGFβ response (F-TBRS) signature (23) and NanoString TGFβ and Wnt signaling signatures (see Supplementary Fig. S2E). **G,** Correlation between NanoString "CD8 T cells" and F-TBRS (left) or NanoString TGFβ signaling (right) signature expression. *, $P < 0.05$; **, $P < 0.01$; ***, $P < 0.001$; ****, $P < 0.0001$; ns, nonsignificant.

observed *in vitro* (Supplementary Fig. S4C and S4D), coimplantation with CAFs has no effect on the expression of the activation/proliferation markers PD-1 and Ki-67 on CD8$^+$ T cells (**Fig. 5D**), nor the abundance of tumor-associated Tregs, neutrophils, and macrophages (Supplementary Fig. S4F), indicating that within the TME, CAFs affect CD8$^+$ T-cell accumulation without directly inhibiting their proliferation or indirectly through promoting the expansion of immunosuppressive cells.

D2A1-m2 tumors exhibit a CD8$^+$ T-cell–excluded phenotype

Although the type and density of immune cells within tumors can predict survival across multiple cancer types (37), accumulating evidence suggests that the spatial distribution of immune cells plays an important role in determining patient survival and sensitivity to ICB treatment (38, 39). Given that the presence of CAFs did not inhibit CD8$^+$ T-cell activation or proliferation within tumors (**Fig. 5D**), we sought next to determine whether CAF abundance was associated with their physical exclusion from the tumor mass. CAF-rich D2A1-m2 tumors, but not CAF-poor D2A1 tumors, are characterized by low levels of centrally located, infiltrating CD8$^+$ T cells and their accumulation at the tumor periphery (**Fig. 5E** and **F**; Supplementary Fig. S5A), a phenotype also evident in spontaneous metastatic lung lesions in D2A1-m2 tumor-bearing mice (Supplementary Fig. S5B). This difference in CD8$^+$ T-cell distribution between the D2A1 and

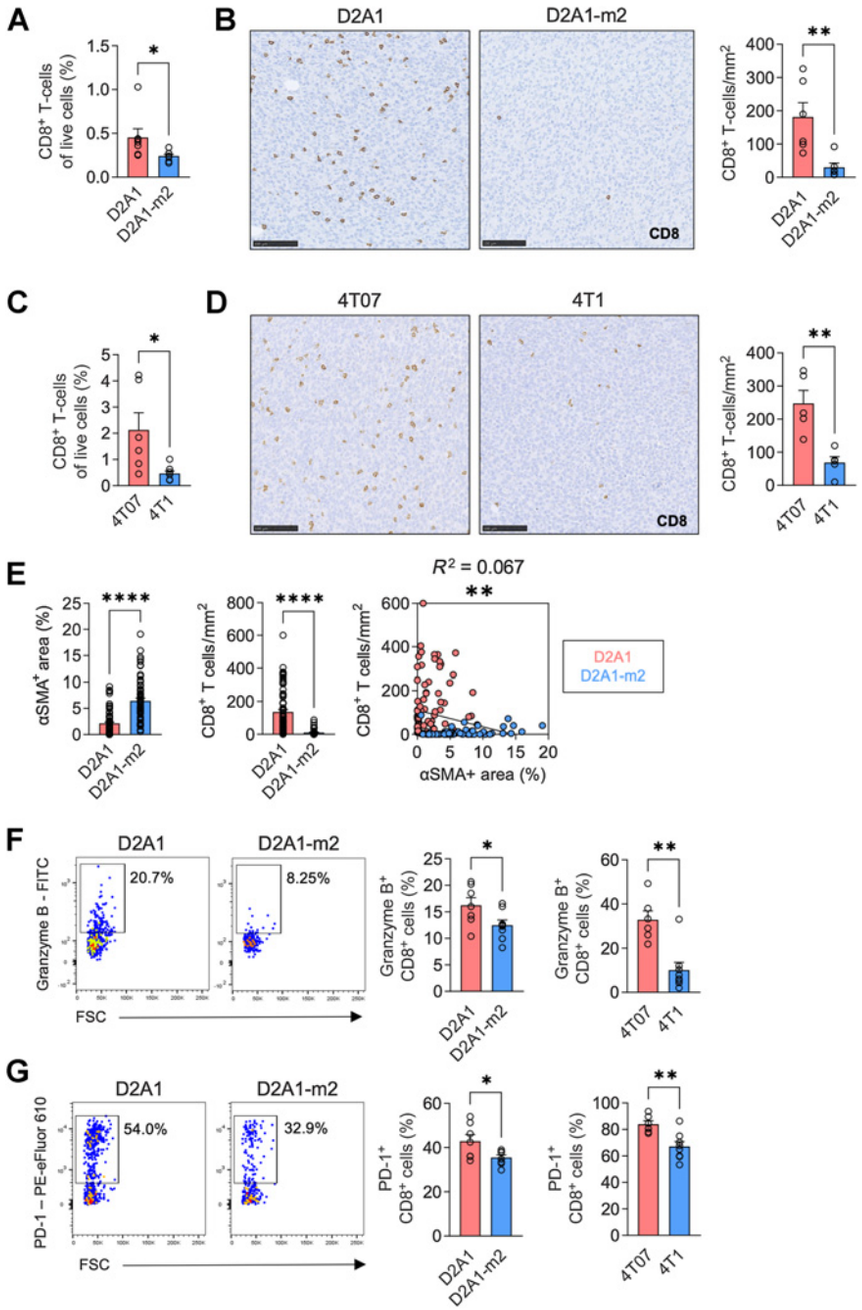

Figure 4.

CAF-rich tumors exhibit an immunologically cold TME. **A–D,** Tumor cells were implanted orthotopically into BALB/c mice. Mice were culled on day 19 (D2A1/D2A1-m2; $n = 7$–8 per group for flow cytometry; $n = 6$ per group for IHC) or day 16 (4T07/4T1; $n = 6$–8 per group for flow cytometry; $n = 5$ per group for IHC; see Supplementary Fig. S3A for tumor weights at necropsy). Left, % $CD8^+$ T cells assessed by flow cytometry (see Supplementary Fig. S3B for gating strategy). Right, IHC analysis. $CD8^+$ T cells per mm^2 tumor section. Representative images. Scale bar, 100 μm. **E,** Quantification of αSMA staining and $CD8^+$ T-cell number in matched 0.25 mm^2 regions from serial sections of D2A1 and D2A1-m2 tumors ($n = 3$ tumors per group; $n = 18$–25 regions per section). Right, correlation of all regions sampled. **F** and **G,** Left, representative pseudocolor dot plots showing the proportion of granzyme B^+ $CD8^+$ cells and PD-1^+ $CD8^+$ cells. Right, granzyme B^+ or PD-1^+ cells as a proportion of $CD8^+$ T cells. *, $P < 0.05$; **, $P < 0.01$; ****, $P < 0.0001$.

D2A1-m2 models persists upon combination αCTLA4 and αPD-L1 treatment, suggesting that ICB treatment alone cannot reverse the $CD8^+$ T-cell-excluded phenotype (**Fig. 5E** and **F**; Supplementary Fig. S5C). Strikingly, ICB treatment significantly increases the overall density of $CD8^+$ T cells in D2A1 tumors, but not in excluded D2A1-m2 tumors (**Fig. 5G**). In neither model does ICB treatment increase CAF abundance (Supplementary Fig. S5D).

Impairment of an Endo180$^+$ CAF subpopulation promotes $CD8^+$ T-cell infiltration and sensitizes tumors to ICB

Characterization of CAFs based on FACS isolation of subpopulations or scRNA-seq has revealed considerable phenotypic and functional diversity (40–43). In a recent study (16), we examined the role of the CAF receptor Endo180 (*Mrc2*) in tumor progression. Endo180 (also known as uPARAP) is a collagen-binding endocytic receptor whose expression is restricted to fibroblasts (Supplementary Fig. S5E) and upregulated on CAFs compared with normal tissue fibroblasts (16). Within CAF subpopulations, the highest levels of Endo180 expression are seen on myCAFs (**Fig. 6A**; ref. 11). Importantly, adult mice with a genetic deletion of Endo180 have no overt phenotype (19, 44), however, when implanted with syngeneic tumor cells show impaired tumor progression (16) and a tumor stroma marked by reduced intratumoral fibrillar collagen content and a depletion in αSMA$^+$ CAFs (**Fig. 6B**).

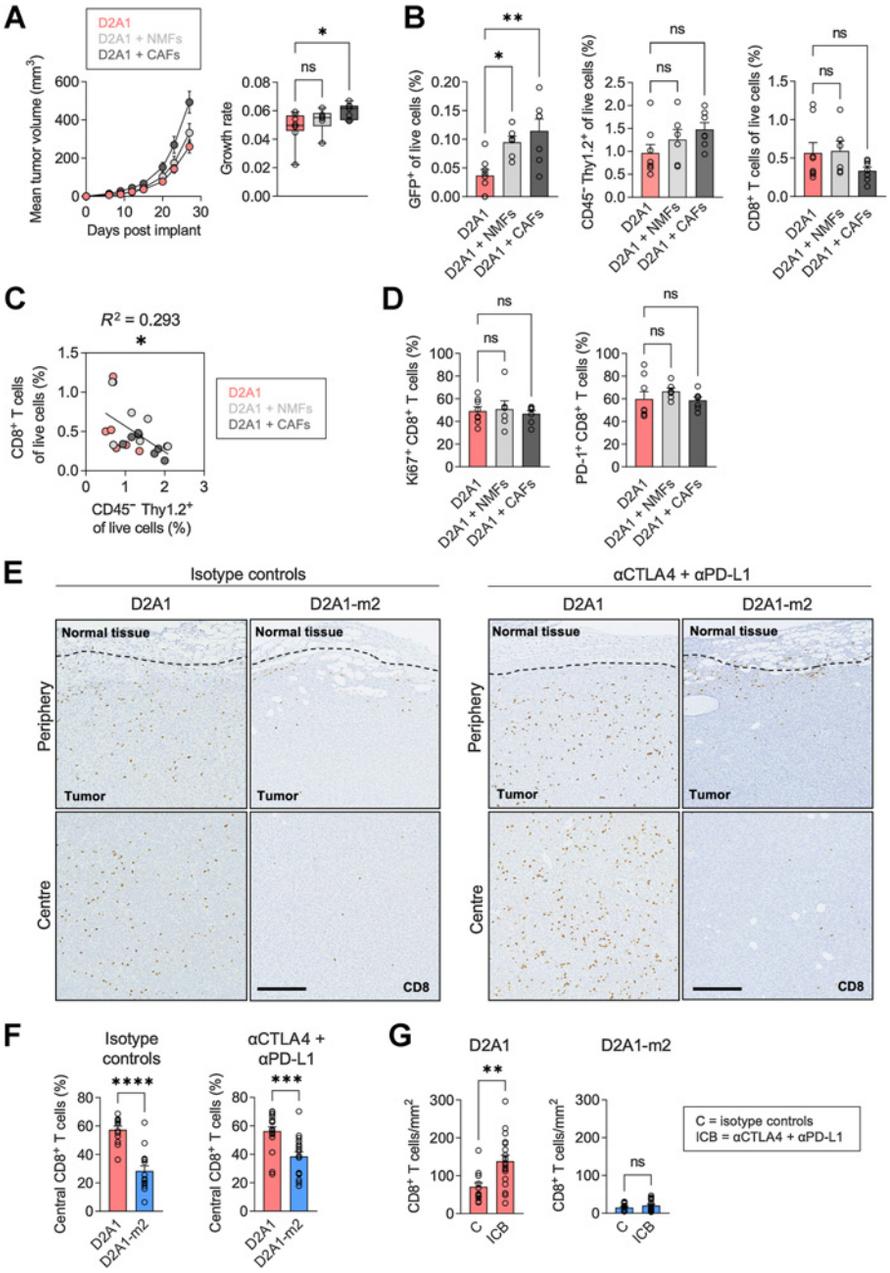

Figure 5.

CD8$^+$ T-cell abundance and distribution in CAF-rich and CAF-poor tumors. **A,** D2A1 cells alone or with GFP$^+$ NMFs or CAFs were implanted orthotopically into BALB/c mice (n = 6–8 mice per group). Tumor growth curves and tumor growth rates. **B–D**, Primary tumors from **A** were analyzed via flow cytometry. **B,** Percentage of live GFP$^+$, CD45-/Thy1.2$^+$, and CD8$^+$ T cells. **C,** Correlation between CD8$^+$ and CD45$^-$/Thy1.2$^+$ cell number in all tumors. **D,** Percentage of Ki67$^+$/CD8$^+$ T cells and PD-1$^+$/CD8$^+$ T cells. **E–G,** D2A1 or D2A1-m2 cells were implanted orthotopically into BALB/c mice (n = 15–18 per group) and treated with αCTLA4 and αPD-L1 antibodies or isotype controls according to the schedule in **Fig. 1E**. **E,** Representative images of peripheral and central regions of tumors from isotype control and ICB-treated mice stained for CD8. Dotted line, tumor stroma boundary. Scale bar, 250 μm. **F,** Percentage of centrally located CD8$^+$ T cells (see Supplementary Fig. S5A for the methodology of central and peripheral CD8$^+$ T-cell quantification). **G,** CD8$^+$ T-cell density in control (C) or ICB-treated tumors. *, $P < 0.05$; **, $P < 0.01$; ***, $P < 0.001$; ****, $P < 0.0001$; ns, nonsignificant.

To test the hypothesis that Endo180+ CAFs play a role in the establishment of a tumor-promoting TME by contributing to CD8+ T-cell exclusion, we first examined CD8+ T-cell distribution in D2A1 tumors, established through orthotopic implantation of tumor cells alone or coimplanted with CAFs transduced with nontargeting (shNTC) or Endo180 targeting (shE180) shRNAs (Supplementary Fig. S5F). Coimplantation with Endo180-expressing CAFs reduces the number of tumor-associated CD8$^+$ T cells and significantly reduces the proportion located centrally, effects that are lost when tumor cells are coimplanted with Endo180-deficient CAFs (**Fig. 6C**; Supplementary Fig. S5G). We addressed the relevance of these findings in human breast cancers from the TCGA data set. Cell type abundance estimates using Consensus^{TME} (25) reveal an inverse correlation between cytotoxic and CD8$^+$ T-cell abundance, and expression of *MRC2* (Endo180) and *ACTA2* (αSMA) in basal-like and HER2-enriched breast cancers, with a similar but weaker correlation with a broader fibroblast signature (Supplementary Fig. S6A). No such correlation is observed in ER$^+$ luminal A or B subtypes, or with endothelial cell abundance in any breast cancer subtype.

Given that the knockout of Endo180 results in reduced intratumoral αSMA$^+$ staining (**Fig. 6B**; ref. 16), it was necessary to address whether loss of Endo180 expression results in an overall reduction of CAFs or preferentially affects a specific CAF subset. mCherry-tagged D2A1-m2 cells were implanted orthotopically into Endo180 wild-type (WT) or knockout (KO) BALB/c mice (**Fig. 6D**). Analysis of the tumors by flow cytometry reveals no differences in CD31$^+$ endothelial cell

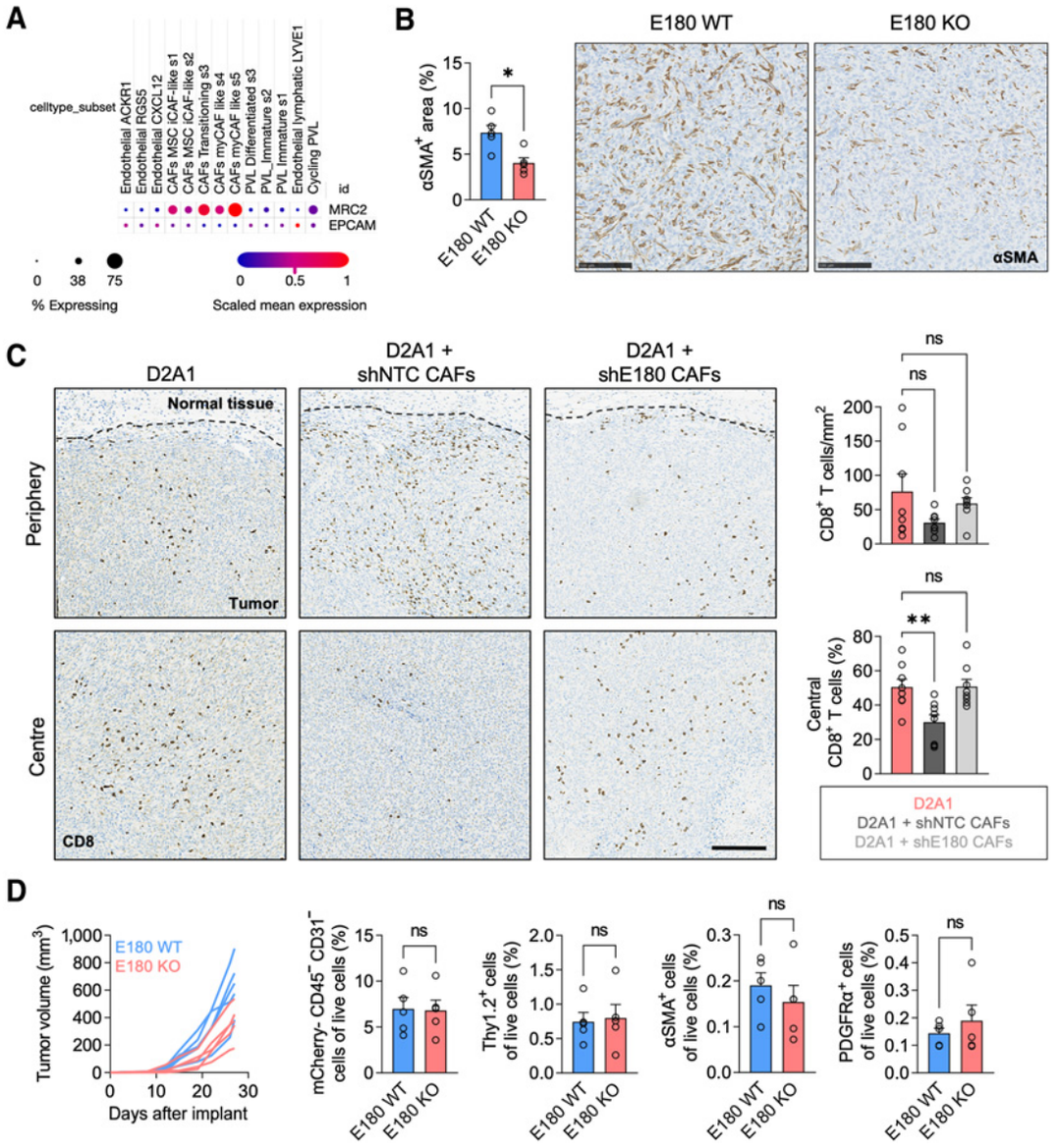

Figure 6.

Functional characterization of Endo180$^+$ CAFs. **A,** Expression of *MRC2* and *EPCAM* in stromal cells from scRNA-seq of 26 human breast cancers (27). **B,** D2A1-m2 cells were implanted orthotopically into Endo180 WT or KO BALB/c mice ($n = 5$ per group). Mice were culled on day 35. Bar chart shows percentage of αSMA$^+$ stained area (mean values per mouse ± SEM, unpaired t test). Representative images. Scale bar, 100 μm. **C,** D2A1 tumor cells were implanted alone or coimplanted with shNTC or shE180 CAFs ($n = 8$ per group; ref. 16). Mice were culled on day 32. Representative images of CD8 IHC in peripheral and central tumor regions. Scale bar, 200 μm. CD8$^+$ T cells per mm^2 and percentage of centrally located CD8$^+$ T cells. **D,** mCherry-tagged D2A1-m2 cells were implanted orthotopically into Endo180 WT or KO BALB/c mice ($n = 5$ per group; ref. 16). Mice were culled on day 27. Left, tumor growth curves. Remaining panels, flow cytometric analysis of indicated stromal cell populations. *, $P < 0.05$; **, $P < 0.01$; ns, nonsignificant.

content, as previously reported (15), or in CD45$^+$ immune cell content (Supplementary Fig. S6B and S6C). Similarly, tumors do not differ in their abundance of total CAFs, defined via negative selection as mCherry$^-$/CD45$^-$/CD31$^-$ cells or by staining with the pan-fibroblast marker Thy1.2 (**Fig. 6D**). Importantly, although there is a reduction in αSMA$^+$ cell abundance in KO tumors, there is a contrasting, nonsignificant increase in PDGFRα$^+$ cells, indicating that Endo180 deletion skews the composition of fibroblast subsets, as has been reported with other interventions (45), without resulting in a general CAF depletion.

To determine whether the reduction in αSMA$^+$ CAFs enhances sensitivity to ICB, D2A1-m2 tumors in WT and KO mice were treated with a combination of αCTLA4 and αPD-L1 antibodies. Consistent with the data in **Fig. 1F**, ICB has no effect on D2A1-m2 tumor growth or survival of WT mice; however, in Endo180 KO mice, ICB treatment significantly suppresses D2A1-m2 tumor growth rate (20%

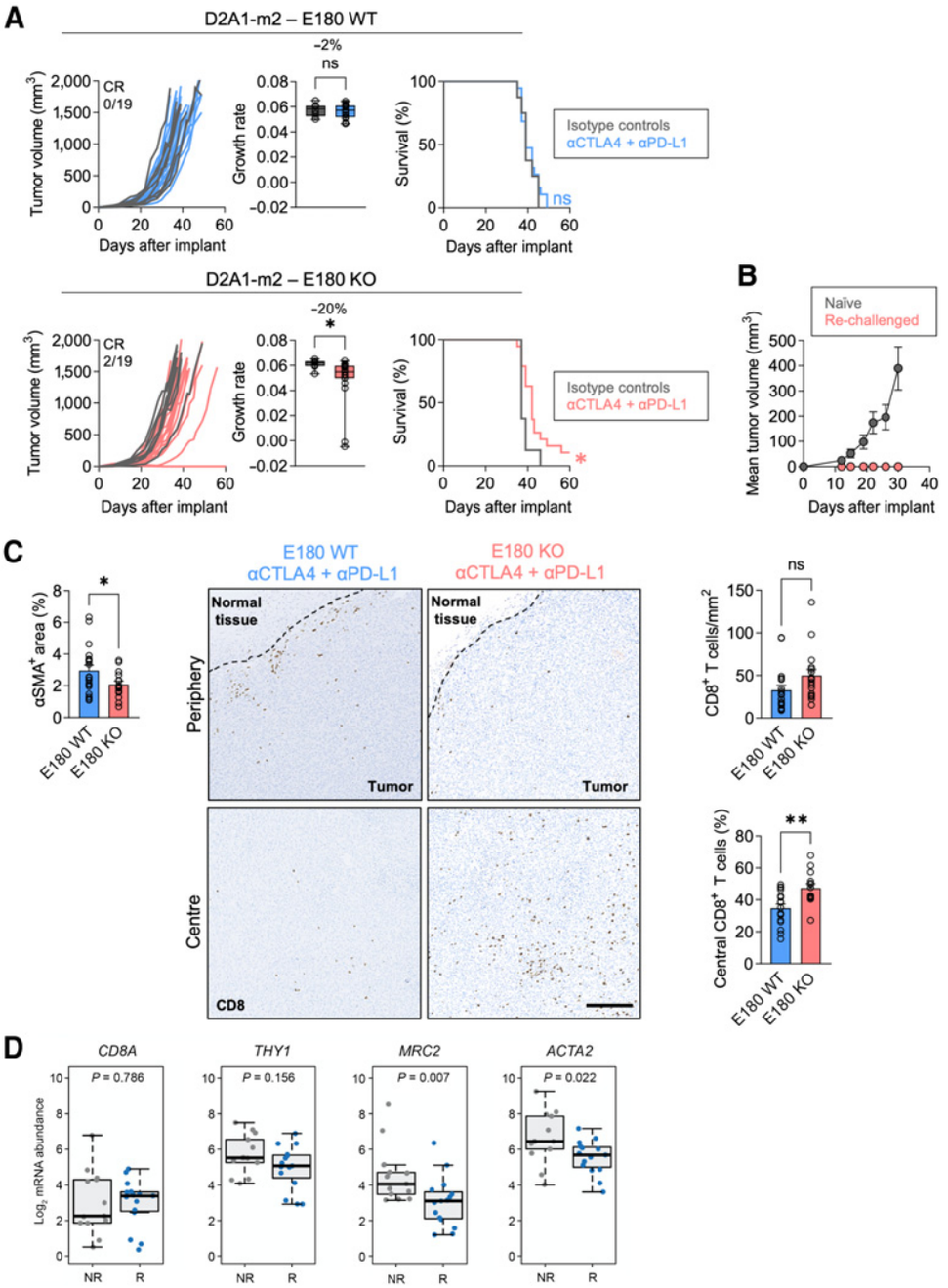

Figure 7.

Stromal Endo180 depletion sensitizes tumors to ICB. **A,** D2A1-m2 cells were implanted orthotopically into Endo180 WT or KO BALB/c mice. Mice were treated with combination αCTLA4/αPD-L1 therapy or isotype control antibodies, according to the **Fig. 1E** schedule ($n = 8$ control and 19 ICB-treated mice per group). Left, tumor growth curves for individual mice. Note, two Endo180 KO ICB-treated mice show complete tumor regression (CR). Middle, tumor growth rates. Right, Kaplan–Meier survival analysis (log-rank test). **B,** D2A1-m2 cells were implanted into the opposite mammary fat pad of the two surviving E180 KO mice from **A** (rechallenged) or into five naïve BALB/c mice. **C,** Tumors from ICB-treated mice from **A** stained for αSMA and CD8. Representative CD8-stained images. Scale bar, 100 μm. Right, total number of $CD8^+$ T cells per mm^2 and percentage of centrally located $CD8^+$ T cells. **D,** mRNA abundance profiles [$\log_2$ (FPKM + 1)] of selected marker genes in melanomas from anti–PD-1 nonresponders (NR) and responders (R; Wilcox rank-sum test; ref. 26). *, $P < 0.05$; **, $P < 0.01$; ns, nonsignificant.

inhibition), extends median survival by 5 days (**Fig. 7A**), and reduces spontaneous metastasis to the lungs (Supplementary Fig. S6D). Remarkably, two ICB-treated KO mice exhibited complete tumor regression and developed an immunologic memory to D2A1-m2 rechallenge (**Fig. 7B**). Quantitative immunohistopathology reveals a significant reduction in αSMA^+ CAFs, an increased number of tumor-associated $CD8^+$ T cells, and a significantly increased proportion of central $CD8^+$ T cells in the KO mice (**Fig. 7C**; Supplementary Fig. S6E), indicating that the impairment of a subset of CAFs can potentiate sensitivity to ICB through optimizing $CD8^+$ T-cell positioning, limiting tumor progression.

Finally, in support of these findings, as no appropriate breast cancer data set exists, we examined a gene expression data set of melanomas for which clinical outcome data following treatment with αPD-1 ICB is available. Gene expression signatures of myCAFs, but not signatures of inflammatory CAFs (iCAF) or normal fibroblasts, are elevated in nonresponders compared with responders (14). In keeping with this report, we show no significant difference in expression of the pan-fibroblast marker *THY1* (CD90) in tumors from responding and nonresponding patients, but a significant elevation in *MRC2* and *ACTA2* expression in nonresponders (**Fig. 7D**).

Discussion

The past decade has seen a rapid expansion of ICB trials in a broad range of cancer types, changing treatment paradigms (1). However, although ICB treatment can result in durable patient responses, there remains an urgent need to understand why success is limited to a minority of patients, and why some cancer types, such as breast cancer, respond particularly poorly. In recent years, an improved understanding of the mechanisms underpinning breast cancer's insensitivity to ICB has provided valuable insight into potential strategies to enhance clinical outcomes (3), with an increasing focus on the role of the TME.

CAFs have been reported to promote the establishment of an immunologically cold TME through both direct modulation of immune cell phenotypes and indirectly via inhibition of immune cell recruitment and infiltration into the developing tumor (9–14). Evidence that this can directly affect sensitivity to ICB has come from strategies directly targeting CAFs or related signaling pathways. For example, inhibiting the ROS-producing enzyme NOX4, which has elevated expression in CAFs, promotes $CD8^+$ T-cell infiltration and enhances response to ICB therapy (46). Similarly, it has been reported that the expression of the proline isomerase Pin1 drives the formation of a desmoplastic CAF-rich stroma in pancreatic adenocarcinomas and reduces PD-L1 expression on tumor cells and that Pin1 targeting reduces desmoplasia and enhances sensitivity to PD-1 blockade (47).

Despite these advances, studies of CAF function have been hampered by three main issues. First, limitations in *in vivo* experimental models where syngeneic models do not adequately represent the genetic and microenvironmental heterogeneity of patient tumors (48). Second, that CAFs cultured *in vitro* alter their phenotype and do not fully represent CAFs *in vivo*, and the caveats associated with the commonly used approach of coimplanting fibroblasts with tumor cells (15). Finally, CAFs, such as tumor cells, represent a heterogeneous population of cells with different functional properties ascribed to different subpopulations (14, 27, 40–43, 49, 50), including both tumor-promoting and tumor-restraining functions (12). To address these experimental limitations, we initiated this project using two pairs of mouse mammary carcinoma cell lines—4T07/4T1 (both derived from the 410.4 cell line) and the D2A1 cell line and its metastatic derivative D2A1-m2—which, when implanted orthotopically into syngeneic mice, give rise to tumors with strikingly different CAF content (17, 29), allowing comparative investigation into the role of a CAF-rich TME on therapeutic responses.

Our findings reveal how CAF-rich models are insensitive to combination ICB treatment and, while poorly infiltrated with $CD8^+$ T cells, do not differ in the infiltration of known immunosuppressive cells nor in their TMB when compared with paired CAF-poor models. The abundance of CAFs in these models is inversely correlated with $CD8^+$ T-cell content, and the CAF-rich models exhibit a $CD8^+$ T-cell-excluded phenotype, providing further evidence to support the exploration of CAF targeting strategies to enhance ICB responses in breast cancer. However, optimal CAF targeting requires the acknowledgment of CAF intra- and intertumoral heterogeneity, targeting specific CAF subpopulations to limit or eliminate CAFs that inhibit CD8+ T-cell recruitment, while retaining CAF populations with tumor-restraining properties.

In a seminal study of the human breast cancer stroma, four CAF subsets were identified that exhibit distinct immunomodulatory properties and accumulate differentially in human breast cancer subsets (43), with the αSMA^{high} CAF-S1 subset, shown to promote the establishment of an immunosuppressive TME and to be enriched in TNBC compared with luminal breast cancers. Subsequent scRNA-seq of CAF-S1 fibroblasts from human breast cancers identified eight clusters, separating into iCAF and myCAF subgroups with an abundance of the three myCAF clusters (ecm-myCAF, TGFβ-myCAF, wound-myCAF), but not the iCAF clusters, associated with reduced $CD8^+$ T-cell infiltration, and being significantly enriched in tumors with primary resistance to αPD-1 treatment (14). myCAF and iCAF populations have also been defined in other tumor types (14, 41). Moreover, consistent with the established role of TGFβ in restricting T-cell infiltration into tumors (23), a signature of the $LRRC15^+$ TGFβ-driven CAF subset, which clusters with the myCAF signature, is associated with poor response to αPD-L1 (50).

Expression of the CAF receptor Endo180 (*Mrc2*) is required for the generation of a tumor-supportive TME, and in preclinical models, its genetic deletion results in the depletion of a subpopulation of αSMA^+ CAFs and a reduction in collagen deposition (16). As bioinformatic analysis demonstrates elevated Endo180 (*MRC2*) expression in human breast cancer myCAFs compared with iCAFs and perivascular fibroblasts, we sought to determine whether modulating Endo180 expression in the CAF-rich, $CD8^+$ T-cell-excluded D2A1-m2 syngeneic breast cancer model could reverse immunosuppression. Using tumor-CAF coimplantation approaches and analysis of tumors from Endo180 KO mice, we provide direct evidence of a role for Endo180-expressing CAFs in promoting an immunologically cold, $CD8^+$ T-cell–excluded tumor phenotype. These preclinical data, combined with analysis of human clinical data sets, provide support for therapeutic modulation of Endo180 in combination with immunotherapy for improving clinical outcomes in CAF-rich breast cancers.

Authors' Disclosures

L. Jenkins reports grants and nonfinancial support from AstraZeneca during the conduct of the study and personal fees from AstraZeneca outside the submitted work. C.M. Isacke reports grants from Biotechnology and Biological Sciences Research Council (BBSRC) and grants from Breast Cancer Now during the conduct of the study. James Harper is a full-time employee of AstraZeneca. Liam Jenkins has been a full-time AstraZeneca employee since September 2020. No disclosures were reported by the other authors.

Authors' Contributions

L. Jenkins: Conceptualization, investigation, writing–original draft, writing–review and editing. **U. Jungwirth:** Investigation, writing–review and editing. **A. Avgustinova:** Investigation, writing–review and editing. **M. Iravani:** Investigation, writing–review and editing. **A. Mills:** Data curation, investigation, writing–review and editing. **S. Haider:** Data curation, supervision, investigation, writing–review and editing. **J. Harper:** Conceptualization, supervision, funding acquisition, investigation, writing–original draft, writing–review and editing. **C.M. Isacke:** Conceptualization, supervision, funding acquisition, investigation, writing–original draft, writing–review and editing.

Acknowledgments

This study was funded by a BBSRC iCASE studentship to ICR and AstraZeneca (BB/M016099/1 to L. Jenkins) and Programme Grants from Breast Cancer Now (S. Haider and C.M. Isacke) as part of Programme Funding to the Breast Cancer Now Toby Robins Research Centre. This work represents independent research supported by the NIHR Biomedical Research Centre at The Royal Marsden NHS Foundation Trust and the Institute of Cancer Research, London. The views expressed are those of the authors and not necessarily those of the NIHR or the Department of Health and Social Care. The authors thank Alan Melcher (ICR) for insightful discussions, Suzanne Isabelle Sitnikova (AstraZeneca) for help with the design and running of the flow cytometry analyses, and the ICR Biological Services Unit and David Vicente for support with the animal work. The authors thank Dr. Ioannis Roxanis and Dr. Naomi Guppy in the Breast Cancer Now Toby Robins Research Centre Nina Barough Pathology Core Facility for pathology support, Dr. Richard Buus in the Breast Cancer Now Toby Robins Research Centre Pathway Profiling Team for running the NanoString panels, and Breast Cancer Now, working in partnership with Walk the Walk, for supporting the work of these two teams and also Dr. Syed Haider's team.

The costs of publication of this article were defrayed in part by the payment of page charges. This article must therefore be hereby marked *advertisement* in accordance with 18 U.S.C. Section 1734 solely to indicate this fact.

Note

Supplementary data for this article are available at Cancer Research Online (http://cancerres.aacrjournals.org/).

Received December 2, 2021; revised April 30, 2022; accepted June 17, 2022; published first June 24, 2022.

References

1. Wei SC, Duffy CR, Allison JP. Fundamental mechanisms of immune-checkpoint blockade therapy. Cancer Discov 2018;8:1069–86.
2. Kalbasi A, Ribas A. Tumour-intrinsic resistance to immune checkpoint blockade. Nat Rev Immunol 2020;20:25–39.
3. Sharma P, Hu-Lieskovan S, Wargo JA, Ribas A. Primary, Adaptive, and acquired resistance to cancer immunotherapy. Cell 2017;168:707–23.
4. Loi S, Michiels S, Adams S, Loibl S, Budczies J, Denkert C, et al. The journey of tumor-infiltrating lymphocytes as a biomarker in breast cancer: clinical utility in an era of checkpoint inhibition. Ann Oncol 2021;32:1236–44.
5. Cortes J, Cescon DW, Rugo HS, Nowecki Z, Im SA, Yusof MM, et al. Pembrolizumab plus chemotherapy versus placebo plus chemotherapy for previously untreated locally recurrent inoperable or metastatic triple-negative breast cancer (KEYNOTE-355): a randomised, placebo-controlled, double-blind, phase 3 clinical trial. Lancet 2020;396:1817–28.
6. Schmid P, Cortes J, Pusztai L, McArthur H, Kummel S, Bergh J, et al. Pembrolizumab for early triple-negative breast cancer. N Engl J Med 2020;382:810–21.
7. Wein L, Luen SJ, Savas P, Salgado R, Loi S. Checkpoint blockade in the treatment of breast cancer: current status and future directions. Br J Cancer 2018;119:4–11.
8. Chen DS, Mellman I. Elements of cancer immunity and the cancer-immune set point. Nature 2017;541:321–30.
9. Harper J, Sainson RC. Regulation of the anti-tumour immune response by cancer-associated fibroblasts. Semin Cancer Biol 2014;25:69–77.
10. Barrett RL, Pure E. Cancer-associated fibroblasts and their influence on tumor immunity and immunotherapy. Elife 2020;9:e57243.
11. Mhaidly R, Mechta-Grigoriou F. Fibroblast heterogeneity in tumor micro-environment: role in immunosuppression and new therapies. Semin Immunol 2020;48:101417.
12. Chen Y, McAndrews KM, Kalluri R. Clinical and therapeutic relevance of cancer-associated fibroblasts. Nat Rev Clin Oncol 2021;18:792–804.
13. Pradhan RN, Krishnamurty AT, Fletcher AL, Turley SJ, Muller S. A bird's eye view of fibroblast heterogeneity: a pan-disease, pan-cancer perspective. Immunol Rev 2021;302:299–320.
14. Kieffer Y, Hocine HR, Gentric G, Pelon F, Bernard C, Bourachot B, et al. Single-cell analysis reveals fibroblast clusters linked to immunotherapy resistance in cancer. Cancer Discov 2020;10:1330–51.
15. Sahai E, Astsaturov I, Cukierman E, DeNardo DG, Egeblad M, Evans RM, et al. A framework for advancing our understanding of cancer-associated fibroblasts. Nat Rev Cancer 2020;20:174–86.
16. Jungwirth U, van Weverwijk A, Evans RJ, Jenkins L, Vicente D, Alexander J, et al. Impairment of a distinct cancer-associated fibroblast population limits tumour growth and metastasis. Nat Commun 2021;12:3516.
17. Jungwirth U, van Weverwijk A, Melake MJ, Chambers AF, Gao Q, Fivaz M, et al. Generation and characterisation of two D2A1 mammary cancer sublines to model spontaneous and experimental metastasis in a syngeneic BALB/c host. Dis Model Mech 2018;11:dmm031740.
18. Schaefer BC, Schaefer ML, Kappler JW, Marrack P, Kedl RM. Observation of antigen-dependent CD8+ T-cell/dendritic cell interactions in vivo. Cell Immunol 2001;214:110–22.
19. East L, McCarthy A, Wienke D, Sturge J, Ashworth A, Isacke CM. A targeted deletion in the endocytic receptor gene Endo180 results in a defect in collagen uptake. EMBO Rep 2003;4:710–6.
20. Karp NA, Wilson Z, Stalker E, Mooney L, Lazic SE, Zhang B, et al. A multi-batch design to deliver robust estimates of efficacy and reduce animal use - a syngeneic tumour case study. Sci Rep 2020;10:6178.
21. Bankhead P, Loughrey MB, Fernandez JA, Dombrowski Y, McArt DG, Dunne PD, et al. QuPath: open source software for digital pathology image analysis. Sci Rep 2017;7:16878.
22. Ritchie ME, Phipson B, Wu D, Hu Y, Law CW, Shi W, et al. limma powers differential expression analyses for RNA-sequencing and microarray studies. Nucleic Acids Res 2015;43:e47.
23. Mariathasan S, Turley SJ, Nickles D, Castiglioni A, Yuen K, Wang Y, et al. TGFbeta attenuates tumour response to PD-L1 blockade by contributing to exclusion of T cells. Nature 2018;554:544–8.
24. Cancer Genome Atlas N. Comprehensive molecular portraits of human breast tumours. Nature 2012;490:61–70.
25. Jimenez-Sanchez A, Cast O, Miller ML. Comprehensive benchmarking and integration of tumor microenvironment cell estimation methods. Cancer Res 2019;79:6238–46.
26. Hugo W, Zaretsky JM, Sun L, Song C, Moreno BH, Hu-Lieskovan S, et al. Genomic and transcriptomic features of response to anti-PD-1 therapy in metastatic melanoma. Cell 2017;168:542.
27. Wu SZ, Al-Eryani G, Roden DL, Junankar S, Harvey K, Andersson A, et al. A single-cell and spatially resolved atlas of human breast cancers. Nat Genet 2021;53:1334–47.
28. Miller FR, Miller BE, Heppner GH. Characterization of metastatic heterogeneity among subpopulations of a single mouse mammary tumor: heterogeneity in phenotypic stability. Invasion Metastasis 1983;3:22–31.
29. Avgustinova A, Iravani M, Robertson D, Fearns A, Gao Q, Klingbeil P, et al. Tumour cell-derived Wnt7a recruits and activates fibroblasts to promote tumour aggressiveness. Nat Commun 2016;7:10305.
30. Kim K, Skora AD, Li Z, Liu Q, Tam AJ, Blosser RL, et al. Eradication of metastatic mouse cancers resistant to immune checkpoint blockade by suppression of myeloid-derived cells. Proc Nat Acad Sci USA 2014;111:11774–9.
31. Mosely SI, Prime JE, Sainson RC, Koopmann JO, Wang DY, Greenawalt DM, et al. Rational selection of syngeneic preclinical tumor models for immunotherapeutic drug discovery. Cancer Immunol Res 2017;5:29–41.
32. Kubli SP, Berger T, Araujo DV, Siu LL, Mak TW. Beyond immune checkpoint blockade: emerging immunological strategies. Nat Rev Drug Discov 2021;20:899–919.

33. DeNardo DG, Ruffell B. Macrophages as regulators of tumour immunity and immunotherapy. Nat Rev Immunol 2019;19:369–82.
34. Raffin C, Vo LT, Bluestone JA. Treg cell-based therapies: challenges and perspectives. Nat Rev Immunol 2020;20:158–72.
35. Binnewies M, Roberts EW, Kersten K, Chan V, Fearon DF, Merad M, et al. Understanding the tumor immune microenvironment (TIME) for effective therapy. Nat Med 2018;24:541–50.
36. Agorku DJ, Langhammer A, Heider U, Wild S, Bosio A, Hardt O. CD49b, CD87, and CD95 are markers for activated cancer-associated fibroblasts whereas CD39 marks quiescent normal fibroblasts in murine tumor models. Front Oncol 2019; 9:716.
37. Galon J, Costes A, Sanchez-Cabo F, Kirilovsky A, Mlecnik B, Lagorce-Pages C, et al. Type, density, and location of immune cells within human colorectal tumors predict clinical outcome. Science 2006;313:1960–4.
38. Gruosso T, Gigoux M, Manem VSK, Bertos N, Zuo D, Perlitch I, et al. Spatially distinct tumor immune microenvironments stratify triple-negative breast cancers. J Clin Invest 2019;129:1785–800.
39. Vihervuori H, Autere TA, Repo H, Kurki S, Kallio L, Lintunen MM, et al. Tumor-infiltrating lymphocytes and CD8(+) T cells predict survival of triple-negative breast cancer. J Cancer Res Clin Oncol 2019;145: 3105–14.
40. Bartoschek M, Oskolkov N, Bocci M, Lovrot J, Larsson C, Sommarin M, et al. Spatially and functionally distinct subclasses of breast cancer-associated fibroblasts revealed by single cell RNA sequencing. Nat Commun 2018;9: 5150.
41. Ohlund D, Handly-Santana A, Biffi G, Elyada E, Almeida AS, Ponz-Sarvise M, et al. Distinct populations of inflammatory fibroblasts and myofibroblasts in pancreatic cancer. J Exp Med 2017;214:579–96.
42. Cremasco V, Astarita JL, Grauel AL, Keerthivasan S, MacIsaac K, Woodruff MC, et al. FAP delineates heterogeneous and functionally divergent stromal cells in immune-excluded breast tumors. Cancer Immunol Res 2018;6:1472–85.
43. Costa A, Kieffer Y, Scholer-Dahirel A, Pelon F, Bourachot B, Cardon M, et al. Fibroblast heterogeneity and immunosuppressive environment in human breast cancer. Cancer Cell 2018;33:463–79.
44. Engelholm LH, List K, Netzel-Arnett S, Cukierman E, Mitola DJ, Aaronson H, et al. uPARAP/Endo180 is essential for cellular uptake of collagen and promotes fibroblast collagen adhesion. J Cell Biol 2003;160:1009–15.
45. Biffi G, Oni TE, Spielman B, Hao Y, Elyada E, Park Y, et al. IL1-induced JAK/STAT signaling is antagonized by TGFbeta to shape CAF heterogeneity in pancreatic ductal adenocarcinoma. Cancer Discov 2019;9:282–301.
46. Ford K, Hanley CJ, Mellone M, Szyndralewiez C, Heitz F, Wiesel P, et al. NOX4 inhibition potentiates immunotherapy by overcoming cancer-associated fibroblast-mediated CD8 T-cell exclusion from tumors. Cancer Res 2020; 80:1846–60.
47. Koikawa K, Kibe S, Suizu F, Sekino N, Kim N, Manz TD, et al. Targeting Pin1 renders pancreatic cancer eradicable by synergizing with immunochemotherapy. Cell 2021;184:4753–71.
48. Olson B, Li Y, Lin Y, Liu ET, Patnaik A. Mouse models for cancer immunotherapy research. Cancer Discov 2018;8:1358–65.
49. Hutton C, Heider F, Blanco-Gomez A, Banyard A, Kononov A, Zhang X, et al. Single-cell analysis defines a pancreatic fibroblast lineage that supports anti-tumor immunity. Cancer Cell 2021;39:1227–44.
50. Dominguez CX, Muller S, Keerthivasan S, Koeppen H, Hung J, Gierke S, et al. Single-cell RNA sequencing reveals stromal evolution into LRRC15(+) myofibroblasts as a determinant of patient response to cancer immunotherapy. Cancer Discov 2020;10:232–53.